The Effect of Deuteration and Homologation of the Lactam Ring of Nirmatrelvir on Its Biochemical Properties and Oxidative Metabolism

Elena Arutyunova,[∇] Alexandr Belovodskiy,*,[∇] Pu Chen, Muhammad Bashir Khan, Michael Joyce, Holly Saffran, Jimmy Lu, Zoe Turner, Bing Bai, Tess Lamer, Howard S. Young, John C. Vederas, D. Lorne Tyrrell, M. Joanne Lemieux,* and James A. Nieman

Cite This: *ACS Bio Med Chem Au* 2023, 3, 528−541

Read Online

ACCESS | Metrics & More | Article Recommendations | Supporting Information

ABSTRACT: This study explores the relationship between structural alterations of nirmatrelvir, such as homologation and deuteration, and metabolic stability of newly synthesized derivatives. We developed a reliable synthetic protocol toward dideutero-nirmatrelvir and its homologated analogues with high isotopic incorporation. Deuteration of the primary metabolic site of nirmatrelvir provides a 3-fold improvement of its human microsomal stability but is accompanied by an increased metabolism rate at secondary sites. Homologation of the lactam ring allows the capping group modification to decrease and delocalize the molecule's lipophilicity, reducing the metabolic rate at secondary sites. The effect of deuteration was less pronounced for the 6-membered lactam than for its 5-membered analogue in human microsomes, but the trend is reversed in the case of mouse microsomes. X-ray data revealed that the homologation of the lactam ring favors the orientation of the drug's nitrile warhead for interaction with the catalytic sulfur of the SARS-CoV-2 M^pro, improving its binding. Comparable potency against SARS-CoV-2 M^pro from several variants of concern and selectivity over human cysteine proteases cathepsin B, L, and S was observed for the novel deuterated/homologated derivative and nirmatrelvir. Synthesized compounds displayed a large interspecies variability in hamster, rat, and human hepatocyte stability assays. Overall, we aimed to apply a rational approach in changing the physicochemical properties of the drug to refine its biochemical and biological parameters.

KEYWORDS: SARS-CoV-2, deuteration, metabolic stability, protease, antivirals, M^pro, 3CL^pro
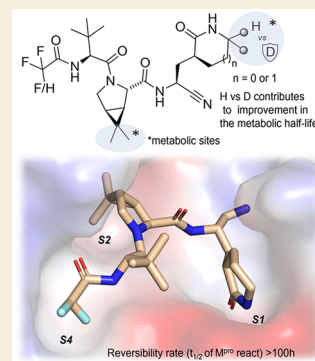
1. INTRODUCTION

Since the COVID-19 outbreak caused by the severe acute respiratory syndrome coronavirus 2 (SARS-CoV-2), major attention from the world scientific community has focused on how to ease its devastating impact on humanity.[1] Although vaccines have been developed, the generation of efficient antiviral treatment is an important component of a multilayered defense system against an infectious disease. Despite numerous drug-discovery efforts targeting both structural and nonstructural proteins of the SARS-CoV-2,[2,3] to date only nirmatrelvir, which is a selective inhibitor of the viral 3-chymotrypsin-like protease (3CL^pro or M^pro), developed by Pfizer, has been approved by FDA. Being the first-in-class drug, nirmatrelvir has a few shortcomings, with low metabolic stability *in vivo* constituting the major drawback.[4] Metabolic stability is a critical aspect in drug development since it increases and prolongs exposure while reducing the number and concentration of metabolites that can impact safety.[5] The ideal drug candidate should be stable enough to reach its therapeutic site of action and maintain a concentration above EC_{90} for a sufficient time period. The liver is the principal site of drug metabolism in the human body, where cytochrome P

(CYP) 450 enzymes in the endoplasmic reticulum membrane clear 70−80% of orally administered drugs.[6]

Inhibition of CYP450 enzymes is one of the strategies that prolongs the half-life of a drug.[7] This approach was used in the case of Paxlovid, which contains nirmatrelvir co-administered with ritonavir, which acts as a CYP3A4 inhibitor increasing the half-life of nirmatrelvir. Ritonavir significantly restricts the safety profile of Paxlovid, because CYP3A4 participates in the metabolism of almost 50% of all clinically used drugs, with half of them relying on this enzyme as a primary means of metabolism.[8−11] This excludes a substantial portion of individuals with pre-existing conditions, who are often susceptible to developing more severe symptoms of COVID-19, from using this antiviral due to potential drug–drug interactions.[12] For this reason, the discovery of second

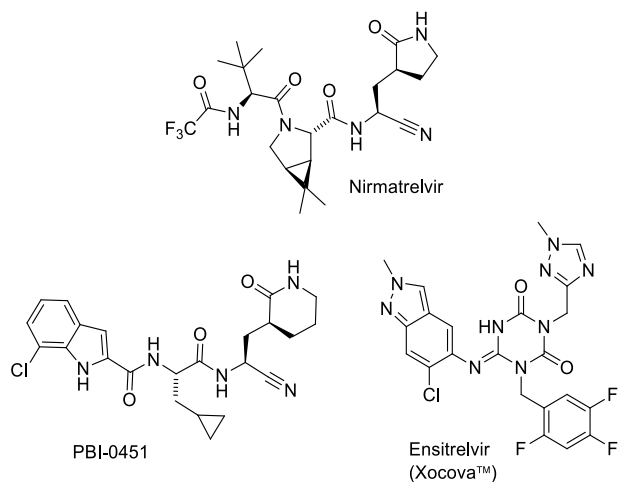generation SARS-CoV-2 antivirals that address metabolic instability is of considerable importance for those at-risk individuals. Currently there are two other 3CL[pro] targeting drugs undergoing late-stage clinical trials for the treatment of SARS-CoV-2 infections, PBI-0451[13] from Pardes and ensitrelvir[14] from Shionogi (Figure 1); the latter was approved for

Figure 1. SARS-CoV-2 M[pro] inhibitors. Approved drugs and treatments undergoing late-stage clinical trials.

emergency use in Japan in November 2022. While ensitrelvir is devoid of the lactam ring that was shown to be the primary metabolism site[4] for nirmatrelvir, PBI-0451 relies on a similar structural motif to mimic a glutamate, and might suffer from the same metabolic shortcomings as Pfizer's drug.[4] Our team has been developing COVID-19 inhibitors from its emergence, exploring peptidomimetics with α-acyloxymethylketone (AMK) warheads[15] and nitrile-warhead based molecules;[16] since our inhibitors revolve around a lactam glutamate mimic like nirmatrelvir and PBI-0451, we explored ways of addressing this metabolic impediment. Since nirmatrelvir is an approved drug, we used it to examine the impacts of the lactam ring size and deuterium incorporation on its oxidative metabolism and other biological properties and to determine whether metabolic stability could be improved so as to not require ritonavir.

Protease specificity nomenclature denotes amino acid residues in a substrate as P3P2P1↓P1′P2′P3′ where the amide bond cleavage occurs between P1 and P1′, as indicated by the arrow. The residues P1′, P1, P2, etc. bind to the specificity pockets of a protease labeled as S1′, S1, S2, etc. Thus, P1 refers to the N-terminal amino acid residue next to the protease cleavage site and is of paramount importance for substrate recognition, which imposes tight constraints on the glutamate mimic in an inhibitor molecule, as revealed in earlier crystal structures.[4,15−18] As a consequence of these constraints, the number of potential approaches[19−21] to improve the metabolic stability of nirmatrelvir is severely limited, because blocking the primary metabolism site, with a methyl or fluorine, will likely reduce inhibitor potency. In the context of such confinements, isotopic incorporation to reduce the rate of P450 oxidation metabolism without impacting potency becomes a favorable option. The kinetic isotope effect is a change in the rate of a reaction upon isotopic substitution, has been known in the field of Organic Chemistry for more than seven decades,[22] and has recently started being applied

successfully in medicinal chemistry and drug development.[23,24] Replacing the hydrogen atom(s) at the site of metabolic oxidation with its heavier stable isotope can theoretically lead to a 2-fold or greater increase in the half-life of a xenobiotic while introducing minimal perturbation to the stereoelectronic portrait of the molecule, preventing any potential negative impact on the compound's activity and/or selectivity. This approach led to the first clinically approved deuterated drug, deutetrabenazine,[25] and has recently been successfully employed in generation of the first de novo deuterated drug deucravacitinib[26] and in development of a remdesivir-inspired nucleoside drug candidate VV116 against SARS-CoV-2.[27,28] Deuteration of an oral HIV protease inhibitor atazanavir, which has to be co-administered with ritonavir for the same reason as nirmatrelvir, led to a 52% increase in half-life in primates[29] and could also prove to be fruitful in the case of SARS-CoV-2 3CL[pro] inhibitors. In the present article, we explore ways of improving the metabolic stability of nirmatrelvir by altering the original molecule and taking advantage of the deuterium kinetic isotope effect (DKIE).

2. MATERIALS AND METHODS

2.1. Expression and Purification of SARS-CoV-2 M[pro]

The M[pro] was expressed and purified as described previously (Genbank: MN908947.3).[30] Briefly, the protein was cloned into the pET-SUMO expression vector resulting in a His-SUMO tag at the N-terminus, transformed into BL21 (DE3) *Escherichia coli*, induced with 0.5 mM isopropyl β-D-1-thiogalactopyranoside, and expressed at 32 °C for 5 h. The protein was purified using Ni-NTA resin (Qiagen, Canada), followed by SUMO-tag removal using His-tagged SUMO protease (McLab, United States) and size exclusion chromatography of the final protein sample on Superdex75 Increase10/300 (Cytiva, Canada). Fractions containing pure M[pro] were pooled, concentrated using an Amicon Ultra-15 (MWCO of 10 kDa), aliquoted, and flash frozen.

2.2. Enzyme Kinetics of M[pro] Protease and Reversibility Studies

Fluorescence resonance energy transfer (FRET)-based enzymatic assays were performed using a synthetic peptide fluorescent substrate containing the cleavage site of M[pro] [Abz-SVTLQ↓SG-Tyr(NO$_2$)-R] as described previously.[28,31] For K_i determination, M[pro] was preincubated with a compound in the concentration range of 0.01−0.2 μM for 10 min, and then Michaelis−Menten kinetics were measured in the presence of each compound concentration with 100 nM M[pro] and 1−600 μM FRET substrate in assay buffer (25 mM Bis-Tris, pH 7.4, 1 mM DTT), containing the corresponding concentration of compound. The fluorescence signal of the FRET peptide cleavage product was monitored at an emission wavelength of 420 nm with excitation at 320 nm, using a Cytation 5 Imaging Multi-Mode Reader (BioTek, USA) for 7 min at 37 °C. The kinetic data were analyzed using computer-fit calculation (Prism 9.0, GraphPad Software). The experiments were performed in triplicate (Figure S1).

For IC$_{50}$ determination, 100 nM M[pro] was incubated with an inhibitor concentration range of 100 to 0.00001 μM in assay buffer for 10 min, and the activity assay was started with the addition of 80 μM FRET substrate. Prism 9.0, GraphPad software, was used to determine the IC$_{50}$.

For reversibility studies, a 3 μM protease sample was incubated with 20 μM inhibitor (final concentration) dissolved in DMSO for 10 min. DMSO at the same concentration (0.4%) was used as a control. After demonstrating the full inhibition of protease by inhibitors by activity measurement, the samples were dialyzed against 50 mM Tris-HCl, pH 7.4, 200 mM NaCl, 5% glycerol, 1 mM DTT for 72 h at room temperature. The dialysis buffer was changed every 3−6 h to ensure that dissociated drug is diluted to a negligible concentration.

The aliquots were taken at specific time points and M^{pro} activity was measured using a FRET-based assay.

For all enzymatic and inhibition assays, the average of at least two independent experiments was used as a mean number. SEM values were calculated using Prism 9.0, GraphPad Software.

2.3. Crystallization and Structure Determination

The M^{pro} was dialyzed against a buffer containing 5 mM Tris-HCl, pH 8.0, 10 mM NaCl overnight at 4 °C. After dialysis, the protein was concentrated to 9 mg/mL and incubated with five-times molar excess of **5** at 4 °C for 2 h to form the complex prior to crystallization. The crystallization of the complex was achieved by mixing 1 μL of protein with 1 μL of reservoir buffer containing 0.1 M HEPES, pH 7.0, 200 mM NaCl, 20% w/v PEG 6000. The crystals were grown in a sitting-drop vapor diffusion system at 18 °C. The crystals were flash frozen in liquid nitrogen with 15% glycerol as cryoprotectant before X-ray diffraction experiments. The data was collected at the Stanford Synchrotron Radiation Light (SSRL) source, beamline 12-2, with Blu-Ice[32] using the Web-Ice interface.

The crystal diffracted the X-rays to 2.0 Å. The data, processed with XDS,[33] belonged to the space group of $P2_12_12$ and contained a single copy of M^{pro} in the asymmetric unit. The crystal structure was solved by molecular replacement using software Phaser MR[34] with the apo-crystal structure of SARS-CoV-2 M^{pro} (PDB: 6WTM, chain A) as a searching model. The ligand was initially fitted using the LigandFit program of Phenix in the density of a precalculated map and modified manually in Coot.[35] The structure was finally refined using Phenix software.[36] The data collection and refinement parameter statistics of the crystal structure of M^{pro} in complex with **5** are summarized in Table S3.

2.4. Chemistry

For more detailed information regarding the chemistry and synthesis of compounds, see Supporting Information (Part 1. Synthesis. Experimental part). All reagents and solvents were used as purchased from commercial sources. Moisture sensitive reactions were carried out under a nitrogen atmosphere in oven-dried glassware. Reactions were stirred at ambient temperature, unless indicated otherwise. Reaction progress was monitored by TLC [precoated silica gel aluminum plates containing a fluorescent indicator (F-254)] with UV (254 nm) or staining (ninhydrin or phosphomolybdic acid) or alternatively by LC/MS. ^{1}H NMR, ^{13}C NMR, and ^{19}F NMR spectra were recorded at ambient temperature, unless indicated otherwise, with a Bruker Avance III 600 MHz NMR spectrometer equipped with Bruker's 5 mm PABBO probe. DEPTQ was run for ^{13}C NMR. Chemical shifts are reported in ppm downfield from tetramethylsilane using residual solvent signals as internal reference for ^{1}H NMR and ^{13}C NMR. For ^{19}F NMR, chemical shifts are reported relative to $CFCl_3$. NMR spectra were processed utilizing an ACD/Spectrus processor (v2016.1.1, ACD/Laboratories Inc.) and Bruker TopSpin 4.0.6. Silica gel column purifications were performed on a Biotage Isolera system with either Biotage or Silicycle cartridges. The LC/MS system used for monitoring the progress of reactions and assessing the purity (absorbance at 210 nm) consisted of a Dionex ULTIMATE 3000 uHPLC module and Thermo Scientific LTQ XL mass spectrometer with electrospray ionization and Ion-Trap type detector (alternating positive−negative mode). Separations were performed with Thermo Scientific Accucore aQ C18 Polar Endcapped LC column (100 mm × 2.1 mm; particle size 2.6 μm, 80 Å). The column was maintained at 30 °C. Commercial HPLC-grade methanol and domestic Millipore (Milli-Q) filtered water used for chromatography were modified by adding 0.1% (v/v) of formic acid. The eluent was delivered with a constant flow rate of 0.400 mL/min; the column was equilibrated for 5 min with the corresponding eluent prior to injection of the sample (1 to 3 μL). The gradient (Eluent A) was methanol−water 45 to 95% in 5.25 min, followed by 5 min of isocratic 95% methanol−water. Purity of the all final compounds was greater than 95% as determined by UV (210 nm), and the corresponding m/z had the correct M + H and/or M − H signal with the appropriate isotope pattern. High Resolution Mass Spectrometry (HRMS) work was done

on an LTQ Orbitrap XL (Thermo Scientific) apparatus operated in the positive mode.

2.5. Cathepsin Purification and Inhibition Assays

pcDNA3.1 plasmids bearing genes of cathepsin B, S, or L (GenBank: M14221.1, M90696.1, and X12451.1) with a 6× His-tag were transfected into Expi293 suspended cells. The proteins were expressed for 3 days after transfection. Expi293 cells and the culture medium were separated by centrifugation. The proteins of interest were purified from the culture medium. The medium was applied on a Ni Sepharose High performance column (Cytiva, Canada). The column was then washed with 10 column volumes of 50 mM Tris-HCl, pH 7.5, 250 mM NaCl, 10% glycerol, 30 mM imidazole buffer and eluted with a 100−500 mM gradient of imidazole in the same buffer. Eluted fractions were analyzed by SDS-PAGE; the samples with protein of interest were pooled and dialyzed against acidic buffer (50 mM CH_3COONa pH 4.5, 150 mM NaCl, 1 mM DTT at 4 °C) for maturation of cathepsins. The final protein sample was then concentrated using an Amicon Ultra-15 filter with a MWCO of 10 kDa, aliquoted, flash frozen, and stored at −80 °C.

For IC_{50} determination, 50 nM cathepsin B, S, or L was incubated with an inhibitor concentration range of 2 mM to 0.1 μM in 50 mM CH_3COONa, pH 5.0, 150 mM NaCl, 1 mM DTT buffer at 37 °C for 10 min, and the activity assay was started with the addition of fluorogenic substrates: cathepsin B substrate (Z-RR-AMC) was used at a concentration of 350 μM, cathepsin S substrate (Z-VVR-AFC) was used at a concentration of 30 μM, and cathepsin L substrate (Ac-FR-AFC) was used at a concentration of 100 μM. The concentrations of substrates were chosen based on K_M values measured by kinetic parameters of cathepsins (Table S2). Prism 9.0, GraphPad Software, was used to determine the IC_{50} values.

2.6. ADME

The ADME experiments were performed at WuXi AppTech (Shanghai) using standard protocols that were described in our previous works.[15,16] Detailed data of ADME experiments are presented in Supporting Information, part 6, in Tables S6−S8.
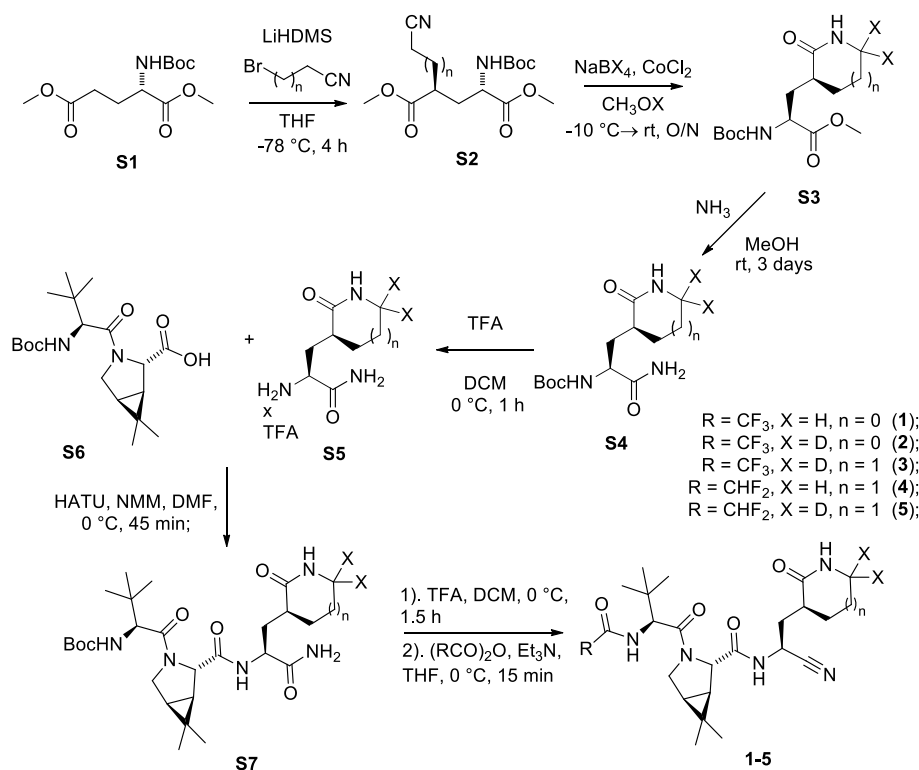
2.7. Microsomal Metabolism/Metabolite Identification Studies

A mixture composed of 5 μL of 20 mg/mL microsomes, 2 μL of 1 mM solution of the test article in acetonitrile, and 183 μL of 100 mM phosphate buffer, pH 7.4, was preincubated at 37 °C while gently shaking for 5 min, then the reaction was initiated with the addition of 10 μL of 30 mM NADPH in 100 mM phosphate buffer. The mixture was incubated for up to 60 min at 37 °C with gentle agitation. The reaction was terminated by mixing a 50 μL aliquot with 50 μL of a 1 μM solution of reserpine in acetonitrile. The samples were vortexed and centrifuged at 15000 rpm for 5 min. Supernatant was analyzed with liquid chromatography−tandem mass spectrometry (LC-MS/MS). Incubations were performed in triplicate. Controls included the following: zero-time point with test article; longest time point, without NADPH; heat-inactivated microsomes (55 °C pretreatment for 30 min); incubation with testosterone. The LC-MS/MS analysis was performed with the Dionex ULTIMATE 3000 uHPLC/Thermo Scientific LTQ XL tandem mass spectrometer as described above. More detailed data for mass-fragmentation of the detected metabolites is provided in Supporting Information, part 4c. The results represent the average of three independent experiments, and SD values were calculated using Prism 9.0, GraphPad Software.

2.8. SARS-CoV-2 Plaque Reduction Assay and Analysis

The EC_{50} and cytotoxicity determinations were carried out using the previously described methods[21] using SARS-CoV-2/Canada/VIDO 01/2020 and Vero E6 cells (Figure S2). Plaques were counted, and data were plotted as the percent inhibition versus $\log_{10}$[compound] using Prism 9.0, GraphPad Software. Assays were performed in duplicate, with the EC_{50} determined with at least five different compound concentrations. EC_{50} values were calculated using a nonlinear regression analysis. For experiments where CP-100356

Scheme 1. Synthesis of Peptidomimetics (1−5)

R = CF$_3$, X = H, n = 0 (**1**);
R = CF$_3$, X = D, n = 0 (**2**);
R = CF$_3$, X = D, n = 1 (**3**);
R = CHF$_2$, X = H, n = 1 (**4**);
R = CHF$_2$, X = D, n = 1 (**5**);

Table 1. Inhibitory and Physicochemical Properties and Microsomal Stability of the Synthesized Derivatives[a]

X = H or D
R = CF$_3$ or CHF$_2$
n = 0 or 1

cmpd	R	X	n	IC$_{50}$, nM	K$_i$, nM	EC$_{50}$,[b] μM	LogD	thermodynamic solubility, μM	microsomal stability, $t_{1/2}$ (min) human	mouse
1	CF$_3$	H	0	33 ± 5	3.1 ± 0.8	1.80 (0.20)	1.86	4790	40.2	14.8
2	CF$_3$	D	0	30 ± 6	3.8 ± 0.2	0.99 (0.06)	1.88	c	117.3	15.5
3	CF$_3$	D	1	41 ± 7	2.1 ± 0.4	0.83 (0.07)	2.09	977	35.5	10.2
4	CHF$_2$	H	1	15 ± 2	3.5 ± 1.0	1.60 (0.10)	1.53	10074	45.5	16.6
5	CHF$_2$	D	1	43 ± 3	3.0 ± 0.9	2.0 (0.04)	1.44	6370	81.6	21.7

[a]Data are presented as mean ± SEM, n = 3. [b]EC$_{50}$ value in the presence of the efflux inhibitor CP-100356 is indicated in brackets. [c]Not determined.

(CP) was added, all procedures were the same except that the media contained 0.5 μM CP.

3. SYNTHESIS

Peptidomimetics (**1−5**) were synthesized for the study as depicted in Scheme 1. Existing synthetic protocols for the nondeuterated inhibitors[4,15,16] were amenable to deuterium introduction by utilizing sodium borodeuteride for the nitrile group reduction in the early stage of the synthetic sequence. A high percentage of deuterium incorporation (>95%) was achieved by conducting the reaction in methanol-OD and using anhydrous cobalt(II) chloride. When the reduction was performed in unlabeled methanol, the degree of deuterium

incorporation did not exceed 60%. The use of anhydrous CoCl$_2$ in place of cobalt(II) chloride hexahydrate had a significantly smaller but still considerable positive effect (Table S1). Once installed, no erosion of the isotope label was observed during subsequent chemical transformations.

Conversion of the ester **S3** into the corresponding primary amide **S4** was achieved by treatment with saturated methanolic ammonia over 3 days (Scheme 1). This approach was found to be superior to the three-step protocol we relied on in the previous work.[16] Our previous method consisted of saponification of the ester with aqueous LiOH, followed by the CDI activation−ammonia treatment cascade and, apart from involving more operations, suffered from loss of the material

during the multiple extraction steps due to considerable aqueous solubility of the intermediates. The "ester-to-primary amide" conversion later in the synthetic scheme with a more lipophilic P1−P2−P3 conjugate resulted in a partial erosion of one of the stereogenic centers of the molecule.

Installation of the tri- or difluoroacetyl group was combined with the primary amide dehydration step by using the corresponding anhydride in excess.

Spectral data for the synthesized derivatives (NMR and HMRS) are provided in Supporting Information, part 5.

4. RESULTS

4.1. Chemical Modifications of Nirmatrelvir and ADME Properties of the Inhibitors

Deuteration is a known chemical modification that helps to reduce the metabolism of certain drugs and may result in improved half-life, safety, tolerability, or efficacy of a compound.[37,38] In addition, we saw a potential for homologation of the γ-lactam ring at P1 of nirmatrelvir, since we demonstrated previously that such a modification in peptidomimetic inhibitors of M[pro] was well tolerated and could improve the potency.[16] We employed both strategies and synthesized two compounds: a deuterated version of nirmatrelvir (**2**) and a deuterated/homologated derivative with the δ-lactam at P1 (**3**). Isotopic replacement for nirmatrelvir had a striking impact on the stability of the compound in the presence of human liver microsomes (Table 1), resulting in an almost 3-fold increase in the half-life from $t_{1/2}$ = 40.2 min for nirmatrelvir (**1**) to $t_{1/2}$ = 117.3 min for deuterated nirmatrelvir (**2**). Mouse microsomes, however, did not noticeably discriminate between nirmatrelvir (**1**) and its deuterated version (**2**). Studies using the homologated analogue (**3**) revealed that this modification leads to a considerable decrease in the metabolic stability of the drug causing its microsomal half-life to drop below that of nirmatrelvir itself ($t_{1/2}$ = 35.5 vs 117.3 vs 40.2 min for **3**, **2**, and **1**, respectively), completely negating the effect of deuteration. This may be due to the higher lipophilicity of analogue **3** (LogD 2.09 vs 1.88);[39,40] however, other explanations such as increased oxidative metabolism of the six-membered ring may also account for decreased microsomal stability. In order to offset the increase in lipophilicity, we synthesized a homologated derivative (**4**) and its deuterated analogue (**5**), where one of the fluorine atoms in the trifluoroacetamide group was replaced with hydrogen. This modification lowered the LogD of the inhibitors to approximately 1.5 and improved their stability in the presence of human [$t_{1/2}$ = 45.5 min for **4** and 81.6 min for deuterated analogue **5**] and mouse microsomes [$t_{1/2}$ = 16.6 and 21.7 min for **4** and **5** vs 10.2 min for inhibitor **3**]. Interestingly, in human microsomes, the difference between isotopic isomers **4** and **5** was less pronounced than for the compounds **1** and **2**, resulting in dideutero-nirmatrelvir **2** having superior human microsomal stability [$t_{1/2}$ = 117.3 min vs $t_{1/2}$ = 81.6 min for **5**], despite its higher lipophilicity.

4.2. Metabolite Identification

We performed Metabolite Identification (MetID) studies on compounds **1** and **4** and their deuterated derivatives **2** and **5** in the presence of both human and mouse microsomes. This allowed us to assess the changes in the metabolites formed by inhibitors with isotopic substitution and homologation. Using LC/MS-MS and MS[3] data, we established the structure of the

main metabolic products for all 4 compounds and measured their relative concentrations (Table 2). In agreement with the

Table 2. Metabolism of Selected Compounds in the Presence of Human Microsomes
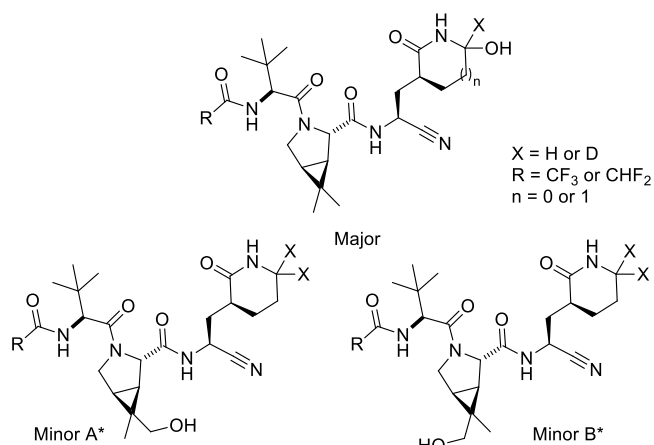
| cmpd | metabolites[a] | | |
	Major	Minor A	Minor B
1	100	5.1 ± 0.8	2.3 ± 0.4
2	39 ± 2	13.4 ± 0.5	6.0 ± 0.6
ratio H/D	2.5 ± 0.1	0.38 ± 0.05	0.39 ± 0.03
4	100	2.4 ± 0.3	2.8 ± 0.1
5	54 ± 7	3.6 ± 0.5	5.1 ± 0.4
ratio H/D	1.9 ± 0.2	0.65 ± 0.01	0.54 ± 0.04

[a]Amount of metabolite in the supernatant after 1 h exposure of the compound to the human microsomes at 37 °C. The amount of the major metabolite for the protic form (**1** and **4**) of the compound was normalized to 100; quantities of all other metabolites are reported relative to the corresponding normalized metabolite. No metabolites were detected in the absence of NADPH or with inactivated microsomes. Data are presented as mean ± SD, n = 3. * in the graphic indicates that the absolute configuration of the new stereogenic center in the metabolites Minor A and Minor B is unknown.

earlier observations by Pfizer,[4,41] the primary site of metabolism for nirmatrelvir in the presence of human microsomes was found to be at the methylene group adjacent to the lactam nitrogen (Major), and two additional minor sites at each of the methyl groups of the cyclopropyl *gem*-dimethyl fragment (Minor A and Minor B) constitute less than 10% of total metabolites (Table 2). A similar oxidation profile was observed for compound **4**, with the major metabolite comprising up to 95% of the total detected oxidation products. We observed significant alterations in the metabolic profile for the deuterated analogues **2** and **5**. Deuteration of the metabolic "soft spot" decreased the amount of the major metabolite by 45−60% with the effect being stronger for nirmatrelvir. At the same time, a noticeable amplification in the oxidation rates at the secondary metabolic sites occurred, leading to formation of larger quantities of minor metabolites A and B. For analogue **5**, the acceleration at the secondary sites of metabolism was within 70% (combined normalized amounts of metabolites A and B increased from 5.2 to 8.7, Table 2). However, deutero-nirmatrelvir (**2**) had significantly higher amounts of minor A and minor B metabolites formed (>200% increase). This can be explained either by decreased accessibility of the major site due to deuteration and thus increased concentration/ availability of sites for minor product formation ("metabolic

switching")[23,42] or product inhibition of the CYP enzymes by the major metabolite or a combination of both factors.

Interestingly, mouse microsomes almost did not discriminate between the deuterated and nondeuterated analogues of nirmatrelvir, with the ratio H/D for the major metabolite being 1.2 ± 0.3 (Table S4), implying that deuteration of **1** reduced the rate of oxidation at that site by only about 20% in mouse microsomes compared to 250% in human microsomes (ratio H/D for **1** = 2.5 ± 0.1, Table 2). For the six-membered lactams **4** and **5** the decrease in the kinetic isotope effect upon transition from the human to mouse microsomes was much less substantial (ratio H/D = 1.6 ± 0.02 in mouse microsomes vs 1.9 ± 0.2 in human microsomes, Table S4 and Table 2), which is in agreement with the half-life trend reported in Table 1. Overall, mouse microsomes are characterized by a much faster metabolism; exposures longer than 30 min resulted in decrease of the concentrations of the main metabolites and appearance of double oxidation products.

4.3. Hepatocyte Stability

Assessment of select derivatives in the hepatocyte stability assay revealed a large interspecies variability (Table 3). For

Table 3. Stability of Select Compounds in the Presence of Hepatocytes

cmpd	hepatocyte stability, $t_{1/2}$ (min)		
	rat	hamster	human
1	244.7	57.4	>433.6
4	139.2	a	>433.6
5	164	>216.8	>433.6

aNot determined.

instance, in rat hepatocytes, nirmatrelvir (**1**) was metabolized slower ($t_{1/2}$ = 245 min) than the deuterated analogue **5** ($t_{1/2}$ = 164 min), which had only a small advantage over its protic version **4** ($t_{1/2}$ = 139.2 min). Hamster hepatocytes, however, displayed a reversed pattern with nirmatrelvir being much more prone to metabolism than **5** ($t_{1/2}$ = 57.4 min vs >216 min). All tested compounds had excellent stability in the presence of the human hepatocytes ($t_{1/2}$ > 433.6 min). It is not uncommon for CYP3A substrates to have a higher rate of metabolism in microsomes compared to that in hepatocytes,[43] and this is often caused by a low passive permeability across the cellular membrane being the limiting factor for metabolism.[44]

4.4. Selectivity against Host Cysteine Proteases

All four novel compounds exhibited high biochemical potency with IC_{50} and K_i values in the same range as nirmatrelvir with a K_i around 3 nM (Table 1). Anticipating that deutero-nirmatrelvir (**2**) will likely display a similar biochemical profile to the parent drug, we focused further investigation on the novel deuterated compound **5**, which bore a few structural alterations and still exhibited high potency and an elevated level of metabolic stability.

Compound **5** demonstrated good selectivity when tested against the most abundant cysteine proteases in animal cells—cathepsins. Cathepsins are lysosomal proteases expressed in all mammalian cells and not only indispensable for normal health and vital for many physiological processes but also implicated in many pathological states.[45]

The IC_{50} values of **1** and **5** for cathepsins B and L were ≥ 100 μM in accordance with the previous results demon-

strated for these cathepsins for nirmatrelvir **1**,[4] whereas the selectivity against cathepsin S was lower with IC_{50} values for **1** and **5** of 26 μM and 42 μM, respectively (Figure S4), which are still 1000-fold higher than their IC_{50} values against M^{pro} protease (Table 4).

**Table 4. IC_{50} Values (μM) of Compounds 1 and 5 with 3 Cathepsins^a**

| cathepsin	compound	
	1	**5**
cathepsin B	≥ 1000	≥ 1000
cathepsin S	26 ± 6	42 ± 8
cathepsin L	≥ 100	≥ 1000

^{a}Data are presented as mean $\pm$ SEM, n = 3.

4.5. Reversibility Studies

The rate constant describing the efficiency of covalent bond formation between compound **5** and the enzyme was k_{inact}/K_i = 1.47×10^5 M^{-1} s^{-1} (Figure S3), consistent with its low K_i value. The reversibility studies revealed that the covalent binding between **5** and M^{pro} is reversible with a reactivation half-time approaching 123 h (Figure 2), which is comparable
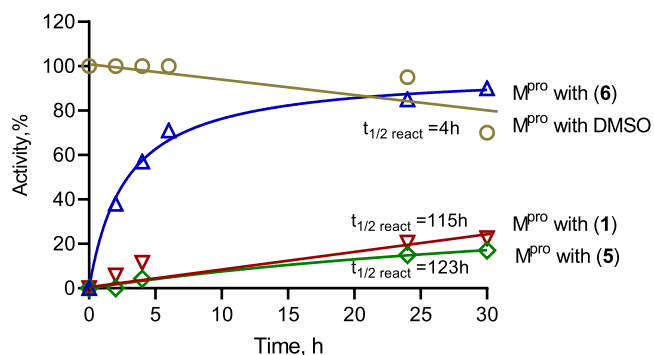

Figure 2. Time course of regained activity of M^{pro} after being incubated with **1**, novel derivative **5**, reported inhibitor **6**, or DMSO as a negative control.

to that of nirmatrelvir (115 h). These values were in striking contrast to the previously reported equipotent M^{pro} inhibitors with the same P1-warhead motif but a Leu for P2 recognition and substituted indole at P3, which have reactivation half-times in a 3−8 h range.[16] To reveal the molecular details of the tight binding of **5**, we compared the structures of M^{pro} complexed with **5** and **1** and with that of inhibitor **6** (Figure 3) previously reported as compound **17a**,[16] which demonstrated comparable activity (IC_{50} = 40 ± 8 nM) but resulted in a much faster off rate ($t_{1/2}$(react) = 4 h) (Figure 2).
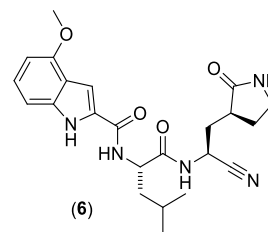
Figure 3. Chemical structure of compound **6**.
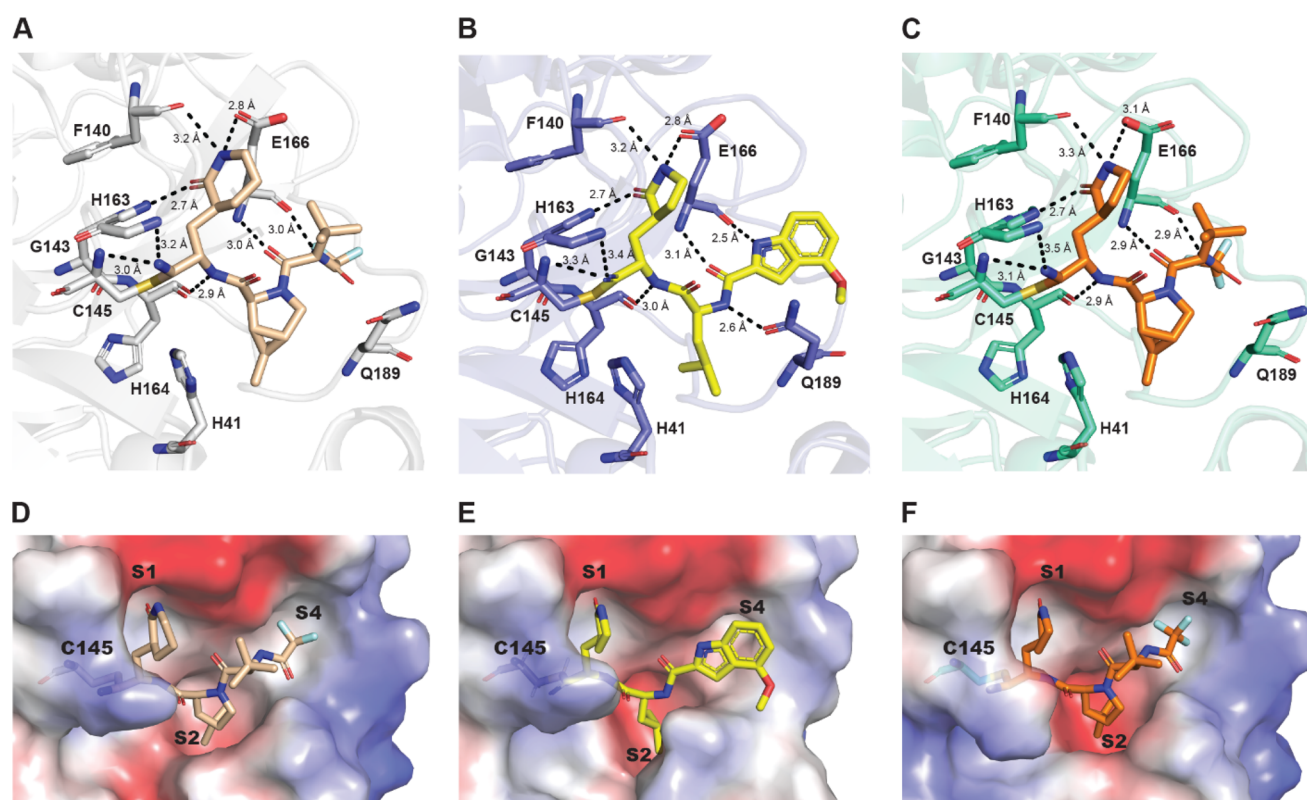
Figure 4. Comparison of the binding modes between SARS-CoV-2 M^pro−**5** (PDB ID: 8FTC), SARS-CoV-2 M^pro−**6** (PDB ID: 7R7H) and SARS-CoV-2 M^pro−**1** (PDB ID: 7RFW). (A) Residues of SARS-CoV-2 M^pro interacting with **5** (wheat sticks) are labeled and shown as gray sticks. (B) Residues interacting with **6** (yellow sticks) are labeled and shown as blue sticks. (C) Residues interacting with **1** (orange sticks) are labeled and shown with green-cyan sticks. All nitrogen atoms are depicted in blue; oxygen atoms are colored in red; and sulfur atoms are colored in bright orange. (D−F) Electrostatic potential surfaces of M^pro in complex with **5**, **6**, and **1**, respectively.

4.6. Comparison of Structures of M^pro in Complex with 1, 5, and 6

To shed light on the molecular basis of the binding mode of **5**, we solved the structure of M^pro complexed with **5** (PDB ID: 8FTC, ligand ID: Y8O). The inhibitor was co-crystallized with the highly purified recombinant protease, and the final model was refined to 2.0 Å resolution. The asymmetric unit contained a single copy of the M^pro molecule. Statistics of data collection, integration, scaling, and structural refinement are summarized in Table S3.

The overall structure of M^pro contains three domains (Figure S5 A). Domain I and domain II share the same antiparallel β-sheet structure and are connected by loop 1 (Val91−Try101) (Figure S5 A). The active site composed of a catalytic dyad Cys145−His41 is located in the groove between domains I and II. Another important catalytic element, an oxyanion hole, is formed by the main element residues Gly143, Ser144, and Cys145 (Figure S6). Domain III, consisting of five α-helices, is connected to domain II by a long loop, which is a part of "active site gateway" comprising two loops, Leu50−Try54 and Asp187−Ala191, the region important for substrate binding (Figure S5A,B). Domain III is also involved in domain swapping to form an active dimer.

To gain insight into the impact of compound binding on the protease molecule, we superimposed our complex structure with the apo-M^pro structure (PDB ID: 6WTM) (Figure S5A). The superimposition aligned 306 Cα atoms with a root-mean-square deviation (RMSD) of 0.6, suggesting no significant conformational changes within the M^pro molecule. The only

structural element that underwent conformational changes was loop 2 (Figure S5B); Glu166 located on that loop formed a hydrogen bond with the P1 lactam nitrogen atom causing the loop to move backward widening the S1 substrate subsite.

The catalytic sulfur of Cys145 attacked the nitrile warhead of **5** forming a covalent bond and generating a thioimidate adduct (Figure 4A,D). The length of the covalent bond is 1.77 Å, which is typical for C−S covalent bonds observed for other cysteine proteases complexed with inhibitors with nitrile warheads.[16] The nitrogen atom of the warhead forms hydrogen bonds with the amide of the catalytic Cys145 and the oxyanion hole residue Gly143. The NH group of the P1 lactam ring is involved in two important hydrogen bonding interactions with the side chain of Glu166 and the backbone carbonyl of Phe140. Additional stabilization of the complex comes via hydrogen bonding between the NH group of the P1−P2 peptide bond and the carbonyl of His164.

The bicyclic leucine mimic at the P2 position was not involved in any interactions; however, it fits well into the negatively charged S2 substrate binding pocket formed by Met49, Met165, His41, and Arg188 (Figure 4D).

The P3 group of the inhibitor formed several hydrogen bonds between the oxygen atom and NH group of inhibitor and backbone of Glu166, whereas the difluoromethyl group of P4 did not interact with any amino acids but fit very effectively into the hydrophobic S4 binding pocket (Figure 4D).

Structural data indicate that the six-membered lactam ring of P1 of compound **5** supports stronger interactions with Glu166 and Phe140 residues compared with the five-membered ring of

1 (Figure 4A). The distances between the NH-group of the lactam ring and oxygen atoms of amino acids are shorter (3.2 and 2.8 Å for **5** versus 3.3 and 3.1 Å for **1**, Figure 4A,C). In addition, more efficient fitting of the δ-lactam ring of **5** also oriented the warhead of the compound in a better way in relation to the catalytic cysteine, shortening the hydrogen bonds between nitrogen and NH group of Gly143 from 3.5 Å for **1** to 3.2 Å for **5** and with the NH group of Cys145 from 3.1 Å for **1** to 3.0 Å for **5**.

Inhibitor **6** in contrast to compounds **1** and **5** possesses an NH group in the P2–P3 peptide bond capable of forming a strong hydrogen bond with the Gln189 side chain of the M^{pro} (Figure 4B). However, despite the fact that the γ-lactam ring of compound **6** in the P1 position made favorable hydrophobic interactions with Phe140 and Glu166 residues, the indole moiety in the P3–P4 position did not protrude into the S4 substrate binding pocket as effectively as smaller CF_3 and CHF_2 groups of **1** and **5** causing a slightly different orientation of the nitrile warhead and thus weaker hydrogen bonding between the warhead and catalytic cysteine (Figure 4D,E,F). Overall, even though there are more hydrogen bonds between the P2 and P3 groups of **6** and the active site residues compared with **1** or **5**, the inability of the bulky indole group to form elaborate hydrophobic interactions with the substrate binding pocket compromises the integrity of the binding and could be responsible for the higher off rate of **6**. Another reason for the almost 30-fold difference in the reversibility between equipotent inhibitors could lie in accumulation of conformational compromises leading to suboptimal geometry for the inhibitor when inside the binding pocket. For example, visual assessment of the geometry of **6** bound to the M^{pro} reveals that there is a considerable distortion of the H–N–C–C dihedral angle for the P2 leucine (3.4° vs 49.1° for the free ligand after energy minimization) where the side chain is forced to assume an energetically less favorable eclipsed conformation relative to the N–H bond. Software assisted[46] energetic profiling of the geometry of ligand **6** when cocrystallized with M^{pro} revealed that there is a significant amount of cumulative strain in the inhibitor resulting from suboptimal bond lengths, angles, and torsion strains, with the former giving the largest impact. Elimination of those strains by preforming AMBER12[47] energy minimization on the freed ligand decreased the potential energy of the molecule by almost 90%. Thus, disassociation of this inhibitor from the enzyme is accompanied by a significant release of conformational strain of the inhibitor, which could serve as a driving force responsible for the faster off rate of **6** when compared with that of **1** or **5**; it is worth noting that no conformational energy gain was observed for nirmatrelvir and the novel derivative **5** in analogous computation.

4.7. Effect of Mutations in M^{pro} of VOCs on the Potency of Inhibitors

A very important concern for any drug against a viral protein is the development of resistance due to the natural capacity of viruses to mutate in order to adapt to a new host or environment. The emergence of new variants of concern (VOC) bearing mutations in M^{pro} protease despite its high degree of conservation[48] also raised concern for continued efficacy of nirmatrelvir and its derivatives.

Our previous report demonstrated the effect of mutations in M^{pro} from four VOCs on protease activity against viral and host substrates and furthermore showed no change in potency

for nirmatrelvir.[49] To ensure that modifications in the chemical structure of **1** did not affect its ability to inhibit M^{pro} from VOCs, we chose several variants with mutations close to the binding site of the drug.

L50F mutation is found in all VOCs with the highest prevalence in the Delta variant. It is located on the gateway loop in domain I (Figure 5). The crystal structure of M^{pro}
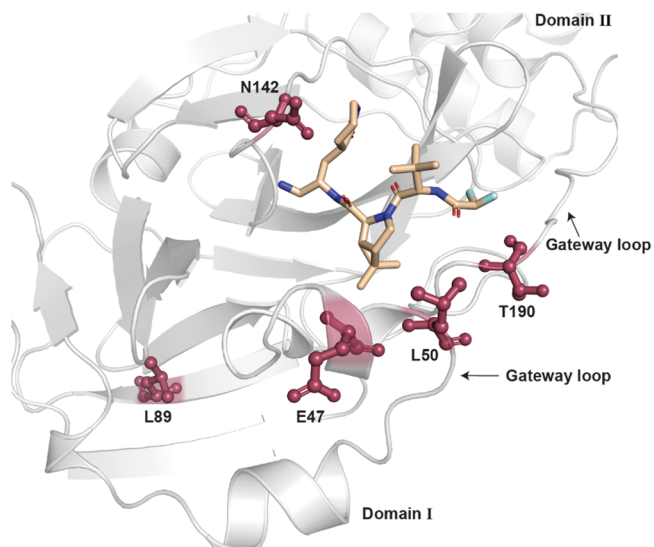
Figure 5. Residues around the active site (shown in burgundy) were mutated in SARS-CoV-2 VOC. The bound compound **5** is shown as wheat sticks (PDB ID: 8FTC).

L50F resulted in loss of charge of the S2 substrate binding site and different orientations of side chains of Met49 and Arg188 residues involved in formation of the S2 pocket. We assume that the hydrophobic surface of the S2 pocket of M^{pro} of the L50F mutant forms more favorable interactions with P2 groups of **1** and **5** compounds, which is reflected in their lower IC_{50} values for this variant (Table 5).

Table 5. IC_{50} Values (nM) for Wild-Type and Mutants of M^{pro} for 5 and 1[a]

M^{pro} mutant	compound	
	1	**5**
wild-type	33 ± 5	43 ± 6
E47N	22 ± 3	7 ± 1
E47K	28 ± 4	4 ± 0.7
L50F	17 ± 2	7 ± 1.3
L89F	32 ± 2	19 ± 0.6
N142S	38 ± 7	29 ± 5
T190I	29 ± 8	16 ± 4

[a]Data are presented as mean ± SEM, n = 3.

More significant changes were observed with the M^{pro} E47 residue, located in close proximity to important elements of the active site, the catalytic histidine and gateway loop, and it has two substitutions in VOC, to Asn and to Lys (Figure 5). Mutation to Asn was found with a high prevalence in Alpha SARS-CoV-2 VOC, whereas substitution to Lys was found in all four VOC but occurred with a low frequency. As we reported previously, in addition to the alteration of the side chain orientation of several residues involved in S2, S3, and S4

pockets (Met49, Met165, Glu166, and Gln189), the M^{pro} E47N variant had a drastic change in shape and charge of the S4 pocket.[45] Its strong negative charge contributed to the binding with hydrophilic CHF$_2$ group and resulted in 5−10-fold lower IC$_{50}$ values; however, CHF$_2$, while capable of acting as a hydrogen bond donor,[50] did not form any specific interactions.

The structure of the E47K variant did not reveal any differences in the S4 site; however, the decrease in IC$_{50}$ can be explained by tighter interaction of the compound within the S2 pocket, which became more hydrophobic in this variant.

T190I mutation is also a part of the gateway loop in domain II (Figure 5) and was found mostly in Alpha and Delta SARS-CoV-2 variants. The mutation did not cause significant changes in the crystal structure of the protease and did not change the IC$_{50}$ values for **1** and **5**. The same tendency for IC$_{50}$ values was observed for the N142S mutant, found in the Delta variant. Located on the loop, which is involved in interaction with P1 position, N142S still did not cause any disruptions in binding of either compound. Lastly, the M^{pro} L89F mutation was chosen as a control. Found in all VOCs, L89 residue did not participate in inhibitor coordination (Figure 5) and as expected did not significantly influence the interaction of compounds with the active site.

5. DISCUSSION

Optimization of the chemical structure of a drug candidate is not a trivial process and includes finding the right balance in the physicochemical properties to enhance the pharmacokinetic profile without compromising the inhibitor's potency and selectivity. Modern medicinal chemistry has a large arsenal of strategies to ameliorate the metabolic stability of a drug substance and could range from "scaffold hopping", when the whole chemical nature of an inhibitor is redesigned bearing in mind some key pharmacophore interactions, to surgical microadjustments like site-specific replacement of a hydrogen atom with fluorine.[51,52] Oftentimes, the identification of a metabolic "soft spot" is followed by attempts to remove or replace it, for example, by using bioisosteres, to sterically hinder or block the site of metabolism. There are also some universal "solutions" like reduction of the compound's lipophilicity, which almost always enhance the metabolic stability but could impair its permeability and bioavailability. Frequently, a combination of several tactics is required for success.

Such a combination approach to modify the chemical structure of nirmatrelvir **1** was explored in this work, as we sought to improve its metabolic stability. First, we incorporated deuterium at the primary site of metabolism. The carbon−deuterium bond is shorter and stronger in comparison to the carbon−hydrogen bond and, normally, takes more energy to break due to a lower vibrational frequency of deuterium.[53] Interestingly, for this reason, deuterated drugs often display lower toxicity due to their slower metabolism and thus formation of fewer toxic metabolites capable of drug−drug interactions. When two metabolically labile hydrogen atoms in compounds **1** and **4** were substituted with deuterium, we observed a 2−3 times improvement in the compound's stability in the presence of human microsomes (Table 1, compared to **2** and **5**, respectively). Another strategy for molecular modification is homologation. However, a tandem solution was required in this case. Increasing the size of the ring in the P1 position by expanding the 5-membered γ-lactam

into a 6-membered δ-lactam resulted in higher lipophilicity, as we observed from LogD and solubility data for compound **3** compared to **1** or **2**, and decreased metabolic stability (Table 1). More lipophilic compounds favor binding contacts with the CYP enzymes via hydrophobic interactions, thus increasing the compound's metabolism. However, at the same time structural data suggests that this substitution benefits the fit of the compound into the active site of M^{pro} protease. When we compared the structures of M^{pro} in complex with **1** and **5** we observed that a 6-membered ring at P1 position resulted in formation of shorter and stronger hydrogen bonds in S1 pocket and better orientation of the warhead in relation to the catalytic cysteine thus forming stronger hydrogen bonds (Figure 4). Our next step was to decrease th elipophilicity of **3** to improve its metabolic characteristics while keeping the 6-membered lactam ring in the P1 position to maintain the strong binding affinity of the δ-lactam ring. The trifluoromethyl group at the P4 position was modified to a more hydrophilic difluoromethyl group. The introduction of fluorine is a frequently used medicinal chemistry strategy to optimize stability against oxidation and acid-mediated degradation processes, lipophilicity, and off-target selectivity, as well as to facilitate cell membrane penetration.[54−56] The CHF$_2$ group has the ability to act as a hydrogen bond donor[46] and fine-tune the physicochemical properties of bioactive molecules.[57] A CF$_3$ to CHF$_2$ modification in compound **5** decreased the LogD value to 1.44 and increased thermodynamic aqueous solubility more than 6 times, in comparison to compound **3**, without considerable impairment of its permeability, as could be seen from the cell-based antiviral data (Table 1). The reduced lipophilicity of **5** also resulted in a 2-fold increase of the compound half-life in the presence of mouse and human microsomes in comparison to **3** and, importantly, also an improvement over **1**, though the effect of deuteration for this scaffold in the presence of human microsomes was still less than for the 5-membered ring glutamate-mimic. This observation might reflect the intrinsic proneness of such a homologue to a faster metabolism. It is conceivable that while the overall lipophilicity of compound **5** is lower than that of **2**, leading to diminished residence times at CYP, the higher hydrophobicity of the P1 portion of the molecule favors its orientation in a way that maximizes the exposure of this fragment to a cytochrome active site. It is also possible, however, that a 6-membered lactam has a higher affinity to the human CYP 3A4 heme pocket than its 5-membered analogue, which may also lead to a reduction in the value of the primary isotope effect $k_{H/D}$. It is interesting that upon transition from human to mouse microsomes a complete inversion in the pattern occurred, resulting in the deuteration effect being more pronounced for the 6-membered lactam while it is almost absent for the smaller 5-membered ring. This indicates that the nature of the heme pocket plays a role in the value of the primary isotope effect; however the lower values of the DKIE could arise from a highly asymmetric nature of the transition state of the C−H/D bond dissociation[58] and does not necessarily imply a higher affinity for a particular type of substrate.

Deuteration at the primary metabolism site led to 1.5−3 times augmentation in the amount of two minor metabolites formed in the presence of human and mouse microsomes, when assessed by Metabolite Identification studies (Table 2 and Table S4). These metabolites correspond to the products of oxidation at the methyl groups of the P2 cyclopropyl *gem-*

dimethyl fragment, which initially comprised 5−8% of the total observed metabolic products. While partial blocking of the major clearance pathway may lead to an increase in the effective concentration of xenobiotic, thus favoring alternative ways for elimination, the large difference in augmentation between the nirmatrelvir (**1**) and analogue **4** (210% vs 70% increase) is unexpected. It is possible that the higher lipophilicity of nirmatrelvir may favor its binding to the metabolizing enzymes, thus promoting its oxidation rates. If this hypothesis is correct then metabolism of the most lipophilic analogue **3** under the same conditions would feasibly produce even larger amounts of these minor metabolites A and B, which could shed light on its poor metabolic stability that we highlighted earlier. However, when the inhibitor **3** was subjected to the metabolic study experiment, instead of increased amounts of the indicated minor metabolites, the formation of novel minor metabolites C and D (products of oxidation at the *tert*-butyl group and oxidation of the six-membered ring at a site other than the methylene group next to the nitrogen, respectively) was observed along with the A and B (Table S5). Unfortunately, these results do not help to assert whether the hypothesis in question is correct or not, as instead of the anticipated behavior, an alternative metabolic pathway was realized; but these data still might provide particular insights into the structure-metabolic stability relationships. For example, the ability of a six-membered lactam ring to undergo another type of oxidative metabolism in addition to the site next to the nitrogen may support the idea that δ-lactam, *ceteris paribus*, has a higher intrinsic proneness for oxidation as no metabolites of this type have been reported for a five-membered lactam ring. It is also conceivable that the more lipophilic capping group [CF_3 in compounds **1**, **2**, and **3**] favors binding of this portion of the inhibitor to the P450 heme pocket more so than the CHF_2. While effective to resist metabolic oxidation itself, it leads to a higher exposure of the neighboring groups to metabolizing enzymes, thus yielding larger amounts of the minor metabolites A, B, and C. Note that while we did not record oxidation of the *tert*-butyl group of nirmatrelvir, formation of this metabolite was reported in the literature,[4] albeit in low abundance. Therefore, introduction of a six-membered lactam likely enhances the metabolism rate at P1, while installation of a less hydrophobic CHF_2 moiety as a capping group decreases the degree of microsomal oxidation at P2 and P3 of the inhibitor. These differences could lead to a large distinction in the inhibitors' metabolism rate depending on the expression levels of particular CYP enzymes or their specificity, especially across different animal species. Indeed, the stability of **5** in the presence of hamster hepatocytes was 4 times higher compared to **1**, but this was reversed in the rat hepatocytes.

The inhibitory properties of **5**, such as K_i and EC_{50}, stayed in the same range as those for **1**. In order to characterize the covalent inhibition of M^{pro} protease by **5** in more detail, we assessed several key parameters, such as rate of covalent bond formation and reversibility of inhibition. The latter is the important characteristic of covalent inhibitors since covalent drugs provide undisputed advantages such as increased residency time at the target molecule, lowering dosage and frequency of administration. There is a requirement for a warhead to display high reactivity but be strictly selective, only forming the covalent bond to the active site when held in the correct orientation by neighboring groups and not during an off-target encounter with reactive groups or active sites of host biomolecules.

Kinetic models describe covalent bond formation as a two-step process that begins with the compound interacting with the protease driven by affinity (represented by K_i) and ends with an inactivation step (k_{inact}). Therefore, we determined the ratio of k_{inact}/K_i, which is the preferred metric to rank potency of different covalent inhibitors against a target[59] and which for **5** was 1.47×10^5 M^{-1} s^{-1}, reflecting its high potency.[60]

The orientation and thus the reactivity of the warhead of a covalent inhibitor can be altered by tuning the network of noncovalent bonds and overall interactions of the molecule. The comparison of reversibility data and structural details of M^{pro} complexed with **1** and **6** supports this concept. Compounds **6** and **1** both have a nitrile warhead and a γ-lactam ring in P1 position and display similar IC_{50} values [57 nM for **6** and 33 nM for **1**]. However, binding of **6** to the M^{pro} protease was almost 30 times more reversible than that of nirmatrelvir (**1**). The half-time of reactivation [$t_{1/2}$(react)] was 4 h for **6** versus 115 h for **1** (Figure 2). Even though the hydrogen bond network between **6** and substrate binding pocket residues is as extensive as for **1**, even with an additional bond forming between Gln189 and the P2 backbone NH group of the drug, the bulky indole at P3 is not able to fit into the S4 subsite like the smaller trifluoromethyl group contributing to a tension for the rest of the drug molecule including the warhead, making the active site−inhibitor bond more prone to break down. This emphasizes the importance drug−target interactions and implies that mutations around the active site can negatively affect the potency of a covalent drug.

Given the high mutagenesis rate of the COVID-19 virus and the emergence of new variants with mutations found even in such a conserved protein as M^{pro}, we sought to assess whether mutations proximal to the active site affected the potency of the inhibitor **5**. We identified several single point mutations in the nsp5 gene from clinical isolates of different SARS-CoV-2 lineages using the GISAID EpiCoV database (https://www.gisaid.org/) and determined the efficacy of compound **5** for them. The IC_{50} values against six M^{pro} mutants demonstrated no decrease in inhibition properties (Table 5); on the contrary, most of the tested mutants resulted in lower IC_{50} values, which could be explained by small changes in charge and hydrogen bond distributions in the mutant molecules, which favored M^{pro} interaction with **5**. Interestingly, the lower IC_{50} values in M^{pro} containing mutations of Leu50 or Thr190 residues imply that the "active site gateway" loops are important for drug binding.

6. CONCLUSION

Four novel derivatives of nirmatrelvir were synthesized: nirmatrelvir with the two most metabolically labile hydrogen atoms replaced with its heavier isotope deuterium and homologated protic or deuterated analogues with an extra CH_2 group in the lactam ring P1, carrying either a CF_3 or CHF_2 group at the P4. All of them displayed activity comparable to the parent drug in biochemical and cellular assays.

Both deuteration and homologation of nirmatrelvir proved to be effective approaches to improve the drug's metabolic stability in the presence of human microsomes; the latter modification, however, must be accompanied by the CF_3 to CHF_2 replacement to compensate for the lipophilicity increase.

Deuteration leads to a 2−3-fold increase in human microsomal stability and has a greater effect when implemented in conjunction with a 5-membered ring rather than a 6-membered ring.

Homologation of the P1 lactam ring of nirmatrelvir enhanced metabolism of this site, potentially due to a combination of increased lipophilicity and introducing additional sites of oxidation; however, it allowed for the replacement of the capping group with a more hydrophilic group, thus delocalizing the molecule hydrophobicity and helping to lower its overall LogD, without impairing the compound permeability (according to the EC_{50} values). This modification led to an alteration in the dynamics of metabolism, which might have larger implications depending on the levels of expression of different CYPs and cause interspecies variability in metabolism. Indeed, the metabolic stability of nirmatrelvir and the six-membered inhibitor **5** differed significantly in the presence of hepatocytes from different species, with the novel derivative being 30% less stable than nirmatrelvir in rat hepatocytes but more than 4 times more stable in hamster hepatocytes.

Based on the structural data, the 6-membered lactam at P1 supports stronger interactions between the inhibitor and the S1 pocket of the enzyme when compared with the 5-membered analogue and allows for a more favorable orientation of the nitrile warhead to form the covalent bond with the catalytic sulfur of protease. Rigidity of P2 of nirmatrelvir and its analogues, as well as the ability of their smaller P3−P4 residues to protrude into the S4 pocket of enzyme, significantly reduced their rate of dissociation from the target; a 30-fold difference in the half-time of protease reactivation was observed when nirmatrelvir and its derivative **5** were compared with the previously reported equipotent reversible covalent M^{pro} inhibitor **6**.

Novel compound **5** displayed 2-fold higher stability in the presence of human microsomes and 4-fold longer half-life in hamster hepatocytes than nirmatrelvir. At the same time, the new analogue is characterized by tighter binding to the target enzyme, high potency against known M^{pro} mutants, and excellent selectivity toward the target protease over the cathepsins B, L, and S.

■ ASSOCIATED CONTENT

Ⓢ Supporting Information

The Supporting Information is available free of charge at https://pubs.acs.org/doi/10.1021/acsbiomedche-mau.3c00039.

> Synthetic procedures, spectral and biochemical characterization of novel compounds, crystallography data, MS fragmentation patterns of metabolites, mouse microsomal stability, and additional ADME data (PDF)

Accession Codes

PDB ID: 8FTC; ligand ID: Y8O. Authors will release the atomic coordinates upon article publication.

■ AUTHOR INFORMATION

Corresponding Authors

Alexandr Belovodskiy − *Li Ka Shing Applied Virology Institute and Department of Medical Microbiology and Immunology, University of Alberta, Edmonton, AB T6G 2E1, Canada*; Email: belovods@ualberta.ca

M. Joanne Lemieux − *Department of Biochemistry, University of Alberta, Edmonton, AB T6G 2H7, Canada; Li Ka Shing Institute of Virology, University of Alberta, Edmonton, AB T6G 2E1, Canada*; ⓞ orcid.org/0000-0003-4745-9153; Email: mlemieux@ualberta.ca

Authors

Elena Arutyunova − *Department of Biochemistry, University of Alberta, Edmonton, AB T6G 2H7, Canada; Li Ka Shing Institute of Virology, University of Alberta, Edmonton, AB T6G 2E1, Canada*; ⓞ orcid.org/0000-0003-4119-3622

Pu Chen − *Department of Biochemistry, University of Alberta, Edmonton, AB T6G 2H7, Canada; Li Ka Shing Institute of Virology, University of Alberta, Edmonton, AB T6G 2E1, Canada*

Muhammad Bashir Khan − *Department of Biochemistry, University of Alberta, Edmonton, AB T6G 2H7, Canada*

Michael Joyce − *Li Ka Shing Institute of Virology and Department of Medical Microbiology and Immunology, University of Alberta, Edmonton, AB T6G 2E1, Canada*

Holly Saffran − *Li Ka Shing Institute of Virology and Department of Medical Microbiology and Immunology, University of Alberta, Edmonton, AB T6G 2E1, Canada*

Jimmy Lu − *Department of Biochemistry, University of Alberta, Edmonton, AB T6G 2H7, Canada; Li Ka Shing Institute of Virology, University of Alberta, Edmonton, AB T6G 2E1, Canada*

Zoe Turner − *Department of Biochemistry, University of Alberta, Edmonton, AB T6G 2H7, Canada;* ⓞ orcid.org/0000-0002-3130-5208

Bing Bai − *Li Ka Shing Applied Virology Institute and Department of Medical Microbiology and Immunology, University of Alberta, Edmonton, AB T6G 2E1, Canada*

Tess Lamer − *Department of Chemistry, University of Alberta, Edmonton, AB T6G 2G2, Canada;* ⓞ orcid.org/0000-0002-1511-4540

Howard S. Young − *Department of Biochemistry, University of Alberta, Edmonton, AB T6G 2H7, Canada*

John C. Vederas − *Department of Chemistry, University of Alberta, Edmonton, AB T6G 2G2, Canada;* ⓞ orcid.org/0000-0002-2996-0326

D. Lorne Tyrrell − *Li Ka Shing Institute of Virology, Li Ka Shing Applied Virology Institute, and Department of Medical Microbiology and Immunology, University of Alberta, Edmonton, AB T6G 2E1, Canada*

James A. Nieman − *Li Ka Shing Applied Virology Institute and Department of Medical Microbiology and Immunology, University of Alberta, Edmonton, AB T6G 2E1, Canada;* ⓞ orcid.org/0000-0002-5087-0819

Complete contact information is available at:
https://pubs.acs.org/10.1021/acsbiomedchemau.3c00039

Author Contributions

[∇]E.A. and A.B. made equal contributions to this work. E.A.: performance/supervision of all biochemical assays, data analysis and interpretation, and 45% of writing of the manuscript. A.B.: development of synthetic protocols and synthesis of compounds (**2**−**5**), performance, analysis and interpretation of MetID studies, conformational strain analysis for the inhibitors (**6**, **5**, and **1**), and 45% of writing of the manuscript. P.C.: crystallization and structural analysis, 10% of writing of the manuscript. M.A.J.: plaque reduction assay

■ LIST OF ABBREVIATIONS

ADME: absorption, distribution, metabolism, and excretion
DCM: dichloromethane
DMF: *N,N*-dimethylformamide
DMSO: dimethyl sulfoxide
ESI: electrospray ionization
Et3N: triethylamine
HATU: hexafluorophosphate azabenzotriazole tetramethyl uranium (1-[bis(dimethylamino)methylene]-1*H*-1,2,3-triazolo[4,5-*b*]pyridinium 3-oxide hexafluorophosphate)
HRMS: high-resolution mass spectrometry
LC: liquid chromatography
LiHMDS: lithium hexamethyldisilazide (lithium bis-{trimethylsilyl}amide)

MeOH: methanol
MS: mass spectrometry
NADPH: nicotinamide adenine dinucleotide phosphate (reduced form)
NMM: *N*-methylmorpholine
NMR: nuclear magnetic resonance spectroscopy
TCEP: tris(2-carboxyethyl)phosphine
TFA: trifluoroacetic acid
THF: tetrahydrofuran

■ REFERENCES

(1) World Health Organization. Global research on coronavirus disease (COVID-19). https://www.who.int/emergencies/diseases/novel-coronavirus-2019/global-research-on-novel-coronavirus-2019-ncov (accessed 1 May 2023).

(2) Mei, M.; Tan, T. Current Strategies of Antiviral Drug Discovery for COVID-19. *Front Mol. Biosci* **2021**, *8*, 13. Sec. Structural Biology

(3) Gil, C.; Ginex, T.; Maestro, I.; Nozal, V.; Barrado-Gil, L.; Cuesta-Geijo, M. A.; et al. COVID-19: Drug Targets and Potential Treatments. *J. Med. Chem.* **2020**, *63* (21), 12359−12386.

(4) Owen, D. R.; Allerton, C. M. N.; Anderson, A. S.; Aschenbrenner, L.; Avery, M.; Berritt, S.; et al. An oral SARS-CoV-2 Mpro inhibitor clinical candidate for the treatment of COVID-19. *Science* **2021**, *374* (6575), 1586−1593.

(5) Masimirembwa, C. M.; Bredberg, U.; Andersson, T. B. Metabolic stability for drug discovery and development: pharmacokinetic and biochemical challenges. *Clin Pharmacokinet* **2003**, *42* (6), 515−28.

(6) Zhao, M.; Ma, J.; Li, M.; Zhang, Y.; Jiang, B.; Zhao, X.; et al. Cytochrome P450 Enzymes and Drug Metabolism in Humans. *Int. J. Mol. Sci.* **2021**, *22* (23), 12808.

(7) Krauß, J.; Bracher, F. Pharmacokinetic Enhancers (Boosters)—Escort for Drugs against Degrading Enzymes and Beyond. *Sci. Pharm.* **2018**, *86* (4), 43.

(8) Ortiz de Monellano, P. R. The Cytochrome P450 Oxidative System. In *Handbook of Drug Metabolism* 3rd ed.; Pearson, P. G., Wienkers, L. C., Eds.; CRC Press: Boca Raton, FL, 2019; Chapter 3, pp 57−82, DOI: 10.1201/9780429190315.

(9) Rendic, S.; Guengerich, F. P. Survey of Human Oxidoreductases and Cytochrome P450 Enzymes Involved in the Metabolism of Xenobiotic and Natural Chemicals. *Chem. Res. Toxicol.* **2015**, *28* (1), 38−42.

(10) Rendic, S. P.; Guengerich, F. P. Human Family 1−4 cytochrome P450 enzymes involved in the metabolic activation of xenobiotic and physiological chemicals: an update. *Arch. Toxicol.* **2021**, *95*, 395−472.

(11) Zanger, U. M.; Schwab, M. Cytochrome P450 enzymes in drug metabolism: Regulation of gene expression, enzyme activities, and impact of genetic variation. *Pharmacology & Therapeutics* **2013**, *138*, 103−141.

(12) Food and Drug Administration. Fact sheet for healthcare providers: emergency use authorization for Paxlovid. https://www.fda.gov/media/155050/download (accessed 1 May 2023).

(13) (a) NIH. U.S. National Library of Medicine, PBI-0451 Phase 2 Study in Nonhospitalized Symptomatic Adults With COVID-19. 16 September 2022, *ClinicalTrials*. https://clinicaltrials.gov/ct2/show/NCT05543707 (accessed 1 May 2023). (b) Pardes Biosciences, Pardes Biosciences Announces Commencement of Phase 2 Trial Evaluating PBI-0451 for the Treatment of SARS-CoV-2 Infections. *Pardesbio*. 13 September 2022, https://ir.pardesbio.com/news-releases/news-release-details/pardes-biosciences-announces-commencement-phase-2-trial (accessed 1 May 2023).

(14) (a) Unoh, Y.; Uehara, S.; Nakahara, K.; Nobori, H.; Yamatsu, Y.; Yamamoto, Y.; et al. Discovery of S-217622, a Noncovalent Oral SARS-CoV-2 3CL Protease Inhibitor Clinical Candidate for Treating COVID-19. *J. Med. Chem.* **2022**, *65* (9), 6499−6512. (b) Sunny, M. E. U.S. NIH starts trial for Shionogi's COVID-19 pill *Reuters*, 16 February 2023, https://www.reuters.com/business/healthcare-

pharmaceuticals/us-nih-starts-trial-shionogis-covid-19-pill-2023-02-15/ (accessed 1 May 2023).

(15) Bai, B.; Belovodskiy, A.; Hena, M.; Kandadai, A. S.; Joyce, M. A.; Saffran, H. A.; et al. Peptidomimetic α-Acyloxymethylketone Warheads with Six-Membered Lactam P1 Glutamine Mimic: SARS-CoV-2 3CL Protease Inhibition, Coronavirus Antiviral Activity, and in Vitro Biological Stability. *J. Med. Chem.* **2022**, *65* (4), 2905−2925.

(16) Bai, B.; Arutyunova, E.; Khan, M. B.; Lu, J.; Joyce, M. A.; Saffran, H. A.; et al. Peptidomimetic nitrile warheads as SARS-CoV-2 3CL protease inhibitors. *RSC Med. Chem.* **2021**, *12*, 1722−1730.

(17) Jin, Z.; Du, X.; Xu, Y.; Deng, Y.; Liu, M.; Zhao, Y.; et al. Structure of Mpro from SARS-CoV-2 and discovery of its inhibitors. *Nature* **2020**, *582*, 289−293.

(18) Zhang, L.; Lin, D.; Sun, X.; Curth, U.; Drosten, C.; Sauerhering, L.; et al. Crystal structure of SARS-CoV-2 main protease provides a basis for design of improved α-ketoamide inhibitors. *Science* **2020**, *368*, 409−412.

(19) Kerns, E. H.; Di, Li. Metabolic Stability. In *Drug-like Properties: Concepts, Structure Design and Methods from ADME to Toxicity Optimization*; Academic Press, 2008; Chapter 11, pp 137−168.

(20) Lima, L. M.; Barreiro, E. J. Bioisosterism: A Useful Strategy for Molecular Modification and Drug Design. *Curr. Med. Chem.* **2005**, *12*, 23−49.

(21) Zhang, Z.; Tang, W. Drug metabolism in drug discovery and development. *Acta Pharm. Sin B* **2018**, *8* (5), 721−732.

(22) Bigeleisen, J.; Mayer, M. G. Calculation of Equilibrium Constants for Isotopic Exchange Reactions. *J. Chem. Phys.* **1947**, *15*, 261−267.

(23) Pirali, T.; Serafini, M.; Cargnin, S.; Genazzani, A. A. Applications of Deuterium in Medicinal Chemistry. *J. Med. Chem.* **2019**, *62*, 5276−5297.

(24) Di Martino, R. M. C.; Maxwell, B. D.; Pirali, T. Deuterium in drug discovery: progress, opportunities and challenges. *Nat. Rev. Drug Discov* **2023**, *22*, 562−584.

(25) Schmidt, C. First deuterated drug approved. *Nat. Biotechnol.* **2017**, *35*, 493−494.

(26) Mullard, A. First de novo deuterated drug poised for approval. *Nat. Rev. Drug Discov* **2022**, *21*, 623−625.

(27) Xie, Y.; Yin, W.; Zhang, Y.; Shang, W.; Wang, Z.; Luan, X.; et al. Design and development of an oral remdesivir derivative VV116 against SARS-CoV-2. *Cell Res.* **2021**, *31* (11), 1212−1214.

(28) Cao, Z.; Gao, W.; Bao, H.; Feng, H.; Mei, S.; Chen, P.; et al. VV116 versus Nirmatrelvir−Ritonavir for Oral Treatment of Covid-19. *N Eng. J. Med.* **2023**, *388*, 406−417.

(29) Morgan, A. J.; Pandya, B. A.; Masse, C. E.; Harbeson, S. L. Old Drugs Yield New Discoveries: Examples from the Prodrug, Chiral Switch, and Site-Selective Deuteration Strategies. In *Drug Repositioning: Bringing New Life to Shelved Assets and Existing Drugs*; Barat, M., Frail, D., Eds; John Wiley & Sons, 2012; Chapter 10, pp 291−343.

(30) Vuong, W.; Khan, M. B.; Fischer, C.; Arutyunova, E.; Lamer, T.; Shields, J.; et al. Feline Coronavirus Drug Inhibits the Main Protease of SARS-CoV-2 and Blocks Virus Replication. *Nat. Commun.* **2020**, *11* (1), 4282.

(31) Vuong, W.; Fischer, C.; Khan, M. B.; Van Belkum, M. J.; Lamer, T.; Willoughby, K. D.; et al. Improved SARS-CoV-2 Mpro Inhibitors Based on Feline Antiviral Drug GC376: Structural Enhancements, Increased Solubility, and Micellar Studies. *Eur. J. Med. Chem.* **2021**, *222*, No. 113584.

(32) McPhillips, T. M.; McPhillips, S. E.; Chiu, H. J.; Cohen, A. E.; Deacon, A. M.; Ellis, P. J.; et al. Blu-Ice and the Distributed Control System: software for data acquisition and instrument control at macromolecular crystallography beamlines. *J. Synchrotron Radiat.* **2002**, *9*, 401−6.

(33) Kabsch, W. XDS. *Acta Crystallogr. D Biol. Crystallogr.* **2010**, *66*, 125−32.

(34) Winn, M. D.; Ballard, C. C.; Cowtan, K. D.; Dodson, E. J.; Emsley, P.; Evans, P. R.; et al. Overview of the CCP4 suite and current developments. *Acta Crystallogr. D Biol. Crystallogr.* **2011**, *67*, 235−42.

(35) Emsley, P.; Lohkamp, B.; Scott, W. G.; Cowtan, K. Features and development of Coot. *Acta Crystallogr. D Biol. Crystallogr.* **2010**, *66*, 486−501.

(36) Echols, N.; Grosse-Kunstleve, R. W.; Afonine, P. V.; Bunkóczi, G.; Chen, V. B.; Headd, J. J.; et al. Graphical tools for macromolecular crystallography in PHENIX. *J. Appl. Crystallogr.* **2012**, *45*, 581−586.

(37) Haberson, S. L.; Tung, R. D. Deuterium in Drug Discovery and Development. In *Annual Reports in Medicinal Chemistry*; Macor, J., Ed., Academic Press, 2011; Chapter 24, pp 403−417, DOI: 10.1016/B978-0-12-386009-5.00003-5.

(38) Russak, E. M.; Bednarczyk, E. M. Impact of Deuterium Substitution on the Pharmacokinetics of Pharmaceuticals. *Annals of Pharmacotherapy.* **2019**, *53* (2), 211−216.

(39) Hopkins, A. L.; Keserü, G. M.; Leeson, P. D.; Rees, D. C.; Reynolds, C. H. The role of ligand efficiency metrics in drug discovery. *Nat. Rev. Drug Discovery* **2014**, *13*, 105−121.

(40) Kiani, Y. S.; Jabeen, I. Lipophilic Metabolic Efficiency (LipMetE) and Drug Efficiency Indices to Explore the Metabolic Properties of the Substrates of Selected Cytochrome P450 Isoforms. *ACS Omega* **2020**, *5* (1), 179−188.

(41) Eng, A.; Dantonio, A. L.; Kadar, E. P.; Obach, R. S.; Di, L.; Lin, J.; et al. Disposition of Nirmatrelvir, an Orally Bioavailable Inhibitor of SARS-CoV-2 3C-Like Protease, across Animals and Humans. *Drug Metab. Dispos.* **2022**, *50* (5), 576−590.

(42) Aprile, S.; Colombo, G.; Serafini, M.; Di Paola, R.; Pisati, F.; Bhela, I. P.; et al. An Unexpected Deuterium-Induced Metabolic Switch in Doxophylline. *ACS Med. Chem. Lett.* **2022**, *13* (8), 1278−1285.

(43) Williamson, B.; Harlfinger, S.; McGinnity, D. F. Evaluation of the Disconnect between Hepatocyte and Microsome Intrinsic Clearance and In Vitro In Vivo Extrapolation Performance. *Drug Metab. Dispos.* **2020**, *48* (11), 1137−1146.

(44) Keefer, C.; Chang, G.; Carlo, A.; Novak, J. J.; Banker, M.; Carey, J.; et al. Mechanistic insights on clearance and inhibition discordance between liver microsomes and hepatocytes when clearance in liver microsomes is higher than in hepatocytes. *Eur. J. Pharm. Sci.* **2020**, *155* (1), No. 105541.

(45) Biasizzo, M.; Javoršek, U.; Vidak, E.; Zarić, M.; Turk, B. Cysteine cathepsins: A long and winding road towards clinics. *Mol. Aspects Med.* **2022**, *88*, No. 101150.

(46) *Molecular Operating Environment (MOE)*, v 2022.02; Chemical Computing Group ULC, 1010 Sherbooke St. West, Suite #910, Montreal, QC, Canada, H3A 2R7, 2023.

(47) (a) Case, D. A.; Darden, T. A.; Cheatham, T. E.; Simmerling, C. L.; Wang, J.; Duke, R. E.; et al. *AMBER 12*; University of California: San Francisco. 2012. (b) Salomon-Ferrer, R.; Case, D. A.; Walker, R. C. An overview of the Amber biomolecular simulation package. *WIREs Comput. Mol. Sci.* **2013**, *3* (2), 198−210.

(48) Lee, J. T.; Yang, Q.; Gribenko, A.; Perrin, B.S.Jr; Zhu, Y.; Cardin, R.; et al. Genetic Surveillance of SARS-CoV-2 Mpro Reveals High Sequence and Structural Conservation Prior to the Introduction of Protease Inhibitor Paxlovid. *mBio* **2022**, *13* (4), e00869−22.

(49) Chen, S. A.; Arutyunova, E.; Lu, J.; Khan, M. B.; Rut, W.; Zmudzinski, M.; et al. SARS-CoV-2 Mpro Protease Variants of Concern Display Altered Viral Substrate and Cell Host Target Galectin-8 Processing but Retain Sensitivity toward Antivirals. *ACS Cent Sci.* **2023**, *9* (4), 696−708.

(50) Sessler, C. D.; Rahm, M.; Becker, S.; Goldberg, J. M.; Wang, F.; Lippard, S. J. CF2H, a Hydrogen Bond Donor. *J. Am. Chem. Soc.* **2017**, *139* (27), 9325−9332.

(51) Lombardino, J. G.; Lowe, J. A., III The role of the medicinal chemist in drug discovery — then and now. *Nat. Rev. Drug Discov* **2004**, *3*, 853−862.

(52) Li, J. J. *Medicinal Chemistry for Practitioners*; John Wiley & Sons, Incorporated, 2020. ProQuest Ebook Central.

(53) Gant, T. G. Using Deuterium in Drug Discovery: Leaving the Label in the Drug. *J. Med. Chem.* **2014**, *57* (9), 3595−3611.

(54) Inoue, M.; Sumii, Y.; Shibata, N. Contribution of Organofluorine Compounds to Pharmaceuticals. *ACS Omega* **2020**, *5* (19), 10633−10640.

(55) Wang, J.; Sánchez-Roselló, M.; Aceña, J. L.; del Pozo, C.; Sorochinsky, A. E.; Fustero, S.; et al. Fluorine in Pharmaceutical Industry: Fluorine-Containing Drugs Introduced to the Market in the Last Decade (2001−2011). *Chem. Rev.* **2014**, *114* (4), 2432−2506.

(56) O'Hagan, D. Understanding organofluorine chemistry. An introduction to the C−F bond. *Chem. Soc. Rev.* **2008**, *37*, 308−319.

(57) Zhang, X.; Ling, L.; Luo, M.; Zeng, X. Accessing Difluoromethylated and Trifluoromethylated cis-Cycloalkanes and Saturated Heterocycles: Preferential Hydrogen Addition to the Substitution Sites for Dearomatization. *Angew. Chem. Int. Ed* **2019**, *58* (47), 16785−16789.

(58) Westaway, K. C. Using kinetic isotope effects to determine the structure of the transition states of SN2 reactions. *Adv. Phys. Org. Chem.* **2006**, *41*, 217−273.

(59) Bauer, R. A. Covalent inhibitors in drug discovery: from accidental discoveries to avoided liabilities and designed therapies. *Drug Discov Today* **2015**, *20* (9), 1061−73.

(60) McWhirter, C. Kinetic mechanisms of covalent inhibition. In *Annual Reports in Medicinal Chemistry*; Ward, R. A., Grimster, N. P., Eds.; Academic Press, 2021; Chapter One, pp 1−31.